Research Square

Preprints are preliminary reports that have not undergone peer review.
They should not be considered conclusive, used to inform clinical practice,
or referenced by the media as validated information.

Enhanced structural stability and lithium-ion diffusion in Ni-rich cathodes via synergistic Al/Nb co-modification

Chengzhou Li
Jiangxi University of Science and Technology
Xingrong Hu
Jiangxi University of Science and Technology
Chunxiang Wang
Jiangxi University of Science and Technology
Hao Zheng
Jiangxi University of Science and Technology
Yichen Song
Jiangxi University of Science and Technology
Zhifeng Li
jxlzfeng@163.com

Jiangxi University of Science and Technology

Research Article

Keywords: lithium-ion batteries, Ni-rich layered cathodes, Al/Nb co-modification, structural stability, Li+ diffusion

Posted Date: November 25th, 2026

DOI: https://doi.org/10.21203/rs.3.rs-11314521/v1

License: This work is licensed under a Creative Commons Attribution 4.0 International License.
Read Full License

Additional Declarations: No competing interests reported.

Enhanced structural stability and lithium-ion diffusion in Ni-rich cathodes via synergistic Al/Nb co-modification

Chengzhou Li, Xingrong Hu, Chunxiang Wang*, Hao Zheng, Yichen Song, Zhifeng Li*

School of Materials Science and Engineering, Jiangxi Provincial Key Laboratory of Power Batteries & Energy Storage Materials, Jiangxi University of Science and Technology, Ganzhou 341000, P. R. China.

Abstract

Ni-rich layered cathodes are promising for high energy density lithium-ion batteries because of their high specific capacity and operating voltage. However, their practical application is hindered by Li^+/Ni^{2+} cation mixing, structural degradation, and interfacial side reactions during cycling. Herein, an Al/Nb co-modified Ni-rich layered cathode with a nominal composition of $LiM_{0.98}Al_{0.01}Nb_{0.01}O_2$ ($M = Ni_{0.88}Co_{0.04}Mn_{0.08}$), was synthesized via a co-precipitation method followed by high temperature solid-state calcination. Structural characterization shows that Al/Nb co-doping preserves the layered framework, slightly enlarges the interlayer spacing, and moderately reduces the tendency of Li^+/Ni^{2+} cation disorder. As a result, the co-modified sample delivers a discharge capacity of 155.33 mAh g^{-1} after 160 cycles at 1 C with a capacity retention of 85.71%, and 148.18 mAh g^{-1} at 5 C with a capacity recovery of 96.28% when the rate returns to 0.2 C. GITT, dQ/dV, and EIS analyses further indicate improved Li^+ diffusion kinetics and mitigated structural/interfacial degradation upon cycling. This work demonstrates that synergistic Al/Nb co-doping is an effective strategy for improving the electrochemical performance of low-Co/high-Ni layered cathodes.

Keywords: lithium-ion batteries; Ni-rich layered cathodes; Al/Nb co-modification; structural stability; Li^+ diffusion

*Corresponding author. E-mail address: jxwchx1979@126.com (Chunxiang Wang), jxlzfeng@163.com (Zhifeng Li).

Introduction

With the rapid development of electric vehicles and large-scale energy storage systems, lithium-ion batteries (LIBs) are required to deliver increasingly higher energy density, longer cycle life, and improved safety [1-3]. As one of the key components determining the energy density and service performance of LIBs, cathode materials have attracted sustained research interest [4]. Among various cathode candidates, Ni-rich layered ternary oxides, generally expressed as $LiNi_xCo_yMn_{1-x-y}O_2$ ($x \geq 0.8$), are considered highly promising for high energy density LIBs because of their high capacity, elevated operating voltage, and reduced cobalt content [5-7]. In particular, increasing the Ni content is an effective approach to further enhance capacity while lowering the use of expensive Co, making low-Co/high-Ni cathodes an important development direction for practical applications [8,9].

Despite these advantages, Ni-rich layered cathodes still suffer from several intrinsic issues that severely limit their long-term electrochemical performance [10-12]. First, the similar ionic radii of Ni^{2+} and Li^+ promote Li^+/Ni^{2+} cation mixing, which reduces the degree of layered ordering, hinders Li-ion transport, and accelerates electrochemical polarization during cycling [13,14]. Second, repeated delithiation/lithiation, especially under high-voltage operation, can induce strong anisotropic lattice variation and trigger phase transitions such as H2–H3 transformation, leading to microcrack formation, structural degradation, and even irreversible transformation from the layered phase to spinel-like or rock-salt phases [15-17]. In addition, the surface of Ni-rich cathodes is chemically reactive, and residual lithium compounds together with unstable surface oxygen environments tend to aggravate parasitic reactions with electrolyte, resulting in interfacial film growth, impedance increase, and capacity decay [18-20]. Therefore, simultaneously enhancing structural stability, suppressing interfacial degradation, and improving Li-ion diffusion kinetics remains a critical challenge for Ni-rich layered cathodes.

To address these issues, a variety of modification strategies have been proposed, including surface coating, bulk doping, single-crystal design, concentration-gradient engineering, and interface regulation [21-24]. Among them, bulk doping has been

widely recognized as an effective and practical approach because it can regulate the crystal lattice and local chemical environment at the atomic scale [25,26]. Through rational selection of dopant species, bulk doping can strengthen metal-oxygen bonding, suppress cation mixing, alleviate detrimental phase transitions, and improve kinetic behavior during cycling [27,28]. Compared with surface modification alone, bulk doping is more advantageous for stabilizing the bulk structure while simultaneously affecting interfacial properties, and is thus particularly attractive for Ni-rich layered cathodes.

Among various dopants, Al and Nb have both shown considerable potential in improving the electrochemical properties of Ni-rich cathodes. Al^{3+} is generally considered beneficial for stabilizing the layered framework because of its strong Al-O bonding and its ability to reduce transition-metal migration, thereby contributing to improved structural integrity during cycling [29-31]. However, Al doping alone is often more effective in structural stabilization than in substantially improving Li-ion transport kinetics [32]. In contrast, Nb^{5+} possesses a high valence state and strong Nb-O bonding, and its incorporation has been reported to expand interlayer spacing, optimize the local lattice environment, and facilitate Li-ion migration [33-35]. Therefore, from the perspective of complementary functionality, Al/Nb co-doping is expected to combine the structural stabilization effect of Al with the kinetic enhancement effect of Nb, offering a feasible route to simultaneously improve structural robustness and electrochemical kinetics in Ni-rich layered cathodes.

Although previous studies have demonstrated the positive effects of Al or Nb single doping on Ni-rich cathodes, systematic investigations on the synergistic effect of Al/Nb co-doping remain relatively limited, especially in low-Co/high-Ni systems [20,36]. More importantly, the correlations among structural ordering, cation-mixing suppression, Li-ion diffusion kinetics, and post-cycling interfacial evolution have not yet been fully clarified through a comprehensive comparison among undoped, singly doped, and co-doped samples. As a result, the underlying mechanism by which Al/Nb co-doping improves the electrochemical performance of Ni-rich cathodes still requires further investigation.

Based on the above considerations, an Al/Nb co-modified Ni-rich ternary cathode material with a nominal composition of $LiM_{0.98}Al_{0.01}Nb_{0.01}O_2$, was synthesized in this work. By comparison with the undoped and singly doped samples, the effects of synergistic Al/Nb co-doping on the structural stability, lithium-ion diffusion behavior, and electrochemical performance of the material were systematically investigated. This study provides a useful reference for the compositional design and performance optimization of low-Co/high-Ni layered cathode materials.

2. Experimental

2.1. Materials

Nickel sulfate hexahydrate ($NiSO_4·6H_2O$, analytical grade, Jinchuan Nickel Salts Co., Ltd.), cobalt sulfate heptahydrate ($CoSO_4·7H_2O$, analytical grade, Shanghai Macklin Biochemical Co., Ltd.), manganese sulfate monohydrate ($MnSO_4·H_2O$, analytical grade, Tianjin Kermel Chemical Reagent Co., Ltd.), lithium hydroxide monohydrate ($LiOH·H_2O$, analytical grade, Shanghai Macklin Biochemical Co., Ltd.), aluminum hydroxide ($Al(OH)_3$, analytical grade, Tianjin Kermel Chemical Reagent Co., Ltd.), and niobium pentoxide (Nb_2O_5, analytical grade, Shanghai Macklin Biochemical Co., Ltd.) were used as received without further purification. Deionized water was used throughout all experiments.

2.2. Synthesis of the precursor and cathode materials

The Ni-Co-Mn hydroxide precursor was synthesized by a co-precipitation method. $NiSO_4·6H_2O$, $CoSO_4·7H_2O$, and $MnSO_4·H_2O$ were dissolved in deionized water at a molar ratio of Ni:Co:Mn = 88:4:8 to form a mixed salt solution with a total metal-ion concentration of 2 mol L^{-1}. A 2 mol L^{-1} NaOH solution and a 2.4 mol L^{-1} $NH_3·H_2O$ solution were used as the precipitating agent and chelating agent, respectively. Before co-precipitation, an appropriate amount of deionized water and $NH_3·H_2O$ was introduced into the reactor to obtain an initial ammonia concentration of 1.2 mol L^{-1}. During the reaction, the mixed salt solution, NaOH solution, and $NH_3·H_2O$ solution were continuously fed into the reactor at 55 °C under stirring at 900 rpm, while the pH was maintained at 11.50 ± 0.03. After the reaction, the slurry was aged for 2 h. The precipitate was washed thoroughly with deionized water and dried at 120 °C for 24 h

to obtain the precursor, $(Ni_{0.88}Co_{0.04}Mn_{0.08})(OH)_2$.

The obtained precursor was mixed with $LiOH \cdot H_2O$ at a molar ratio of Li: TM = 1.05: 1, where TM represents the total metal content. For clarity, M is defined as $(Ni_{0.88}Co_{0.04}Mn_{0.08})(OH)_2$. The pristine sample with a nominal composition of $LiMO_2$ was denoted as NCM. Using $Al(OH)_3$ and Nb_2O_5 as the Al and Nb sources, respectively, the Al-modified, Nb-modified, and Al/Nb co-modified samples with nominal compositions of $LiM_{0.99}Al_{0.01}O_2$, $LiM_{0.99}Nb_{0.01}O_2$ and $LiM_{0.98}Al_{0.01}Nb_{0.01}O_2$ were prepared and denoted as NCM-Al, NCM-Nb, and NCM-Al/Nb, respectively. The powder mixtures were ball-milled in a planetary mill for 4 h, dried at 80 °C, and then ball-milled again for 1 h to improve compositional homogeneity. Subsequently, the obtained powders were calcined in a tubular furnace under flowing oxygen using a two-step heat treatment process: pre-calcination at 500 °C for 3 h, followed by calcination at 750 °C for 15 h. After natural cooling to room temperature, the corresponding Ni-rich layered cathode materials were obtained.

2.3. Materials characterization

The crystal structures of the samples were characterized by X-ray diffraction (XRD, Ultima IV, Rigaku, Japan) using Cu Kα radiation (λ = 1.5406 Å) over a 2θ range of 10–80° at a scanning rate of 2° min^{-1}. Rietveld refinement was performed using GSAS-II software to obtain the lattice parameters and structural information. The morphology and surface features of the samples were observed by scanning electron microscopy (SEM, MIRA 4, TESCAN, Czech Republic). The elemental distribution was analyzed by energy-dispersive X-ray spectroscopy (EDS, Quantax 200 XFlash 6|60, Bruker). The microstructure and lattice fringes were further investigated by high-resolution transmission electron microscopy (HRTEM, JEM-2100F, JEOL, Japan). The surface elemental composition and chemical states were analyzed by X-ray photoelectron spectroscopy (XPS, K-Alpha, Thermo Fisher Scientific, USA). All binding energies were calibrated using the C 1s peak at 284.8 eV.

2.4. Electrochemical measurements

For cathode preparation, poly(vinylidene fluoride) (PVDF) and N-methyl-2-pyrrolidone (NMP) were first mixed at a mass ratio of 1:23 to form the binder solution.

The active material, Super P conductive carbon, and PVDF were then mixed at a mass ratio of 8:1:1 to obtain a uniform slurry. The slurry was coated onto aluminum foil, dried at 120 °C for 1 h, roll-pressed, and punched into circular electrodes with a diameter of 12 mm. The active material loading was approximately 1.8-2.0 mg cm^{-2}. The electrodes were further dried under vacuum at 60 °C for 12 h before use. CR2032 coin-type half-cells were assembled in an argon-filled glove box using lithium metal as both the counter and reference electrode, a polypropylene microporous membrane as the separator, and 1.0 mol L^{-1} $LiPF_6$ dissolved in EC/DMC/EMC (1:1:1 by volume) as the electrolyte. The electrolyte volume in each cell was 60 μL. After assembly, the cells were allowed to rest at room temperature for 8 h before electrochemical testing.

Galvanostatic charge/discharge tests were carried out on a battery test system (CT-4008Tn-5V10mA-HWX, Neware, China). Cyclic voltammetry (CV) and electrochemical impedance spectroscopy (EIS) measurements were performed on an Ivium-Stat electrochemical workstation. CV was conducted in the voltage range of 2.5-4.5 V at a scan rate of 0.1 mV s^{-1}. EIS was measured over a frequency range from 10^6 to 10^{-2} Hz with an AC amplitude of 5 mV. The galvanostatic intermittent titration technique (GITT) was conducted in the voltage range of 2.7-4.3 V using a current pulse of 0.1 C for 10 min followed by a relaxation period of 50 min.

3 Results and discussion

3.1 Structural and morphological characterization

The morphology of the as-prepared $(Ni_{0.88}Co_{0.04}Mn_{0.08})(OH)_2$ precursor is shown in Fig. S1. The precursor secondary particles exhibit a well-defined spherical morphology, and their surfaces are composed of densely packed primary particles. The particles are relatively smooth and compact, with a particle size of approximately 10 μm. In addition, the tap density of the precursor reaches 3.128 g cm^{-3}, indicating favorable particle morphology and packing characteristics. The XRD patterns and enlarged diffraction peaks of the four samples are presented in Fig. 1. All samples can be indexed to a typical α-$NaFeO_2$-type layered structure with the R-3m space group, indicating that the introduction of trace amounts of Al and Nb does not alter the bulk crystal structure of the materials [37]. Meanwhile, the clear splitting of the (006)/(012)

and (018)/(110) peaks confirms that all samples possess a well-ordered layered structure [38]. As shown in Fig. 1b, the (003) diffraction peaks of the doped samples shift toward lower angles to different extents, among which the NCM-Al/Nb sample exhibits the most pronounced shift, suggesting an enlarged interlayer spacing.

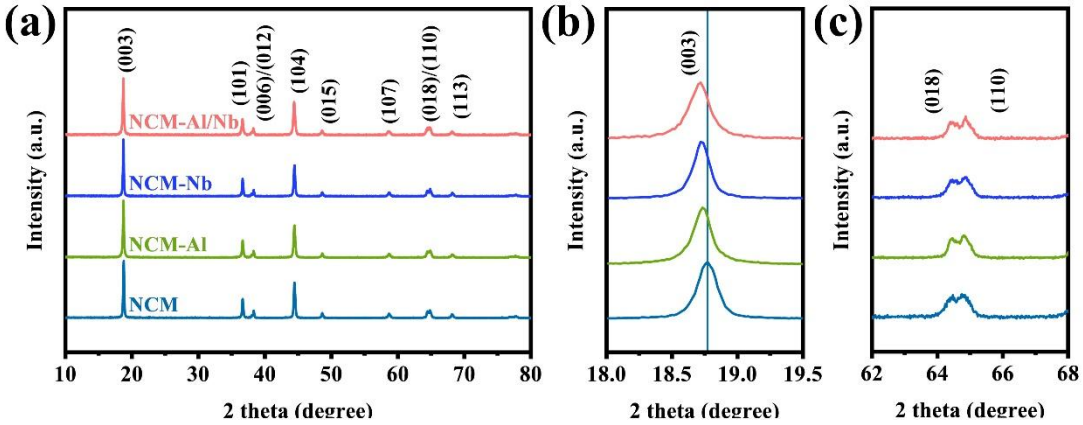


Fig. 1. (a) XRD patterns of the four samples; (b) enlarged view of the (003) peak; (c) enlarged view of the (018)/(110) peaks.

Combined with the Rietveld refinement results (Fig. S2 and Table S1), the NCM-Al/Nb sample shows a larger c-axis lattice parameter, indicating that Al/Nb Co-modification is beneficial for widening the Li^+ diffusion channels in the layered structure and thereby facilitating Li^+ transport [39]. The intensity ratio of $I_{(003)}/I_{(104)}$ is commonly used as an empirical indicator to evaluate the tendency of Li^+/Ni^{2+} cation mixing [40]. All four samples exhibit I(003)/I(104) values greater than 1.2, indicating a relatively low degree of Li^+/Ni^{2+} cation mixing. Compared with the pristine NCM sample, the $I_{(003)}/I_{(104)}$ values of NCM-Al, NCM-Nb, and NCM-Al/Nb increase from 1.59 to 1.74, 1.80, and 1.68, respectively, suggesting that the introduction of Al and/or Nb helps maintain the layered ordering and moderately alleviates Li^+/Ni^{2+} cation disorder compared with pristine NCM. Overall, the NCM-Al/Nb sample exhibits a larger interlayer spacing while maintaining a low Li^+/Ni^{2+} cation-mixing tendency, which provides a favorable structural basis for its improved Li^+ transport kinetics and cycling stability.

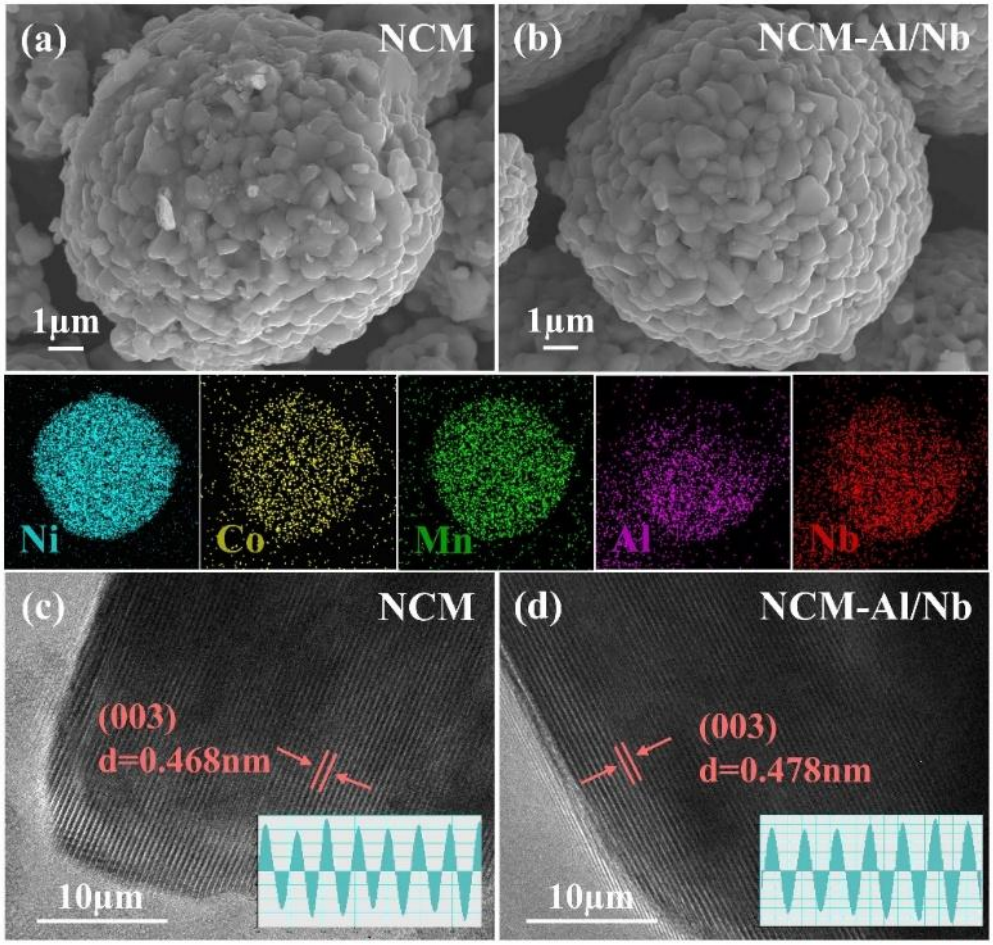


Fig. 2. SEM images of (a) NCM and (b) NCM-Al/Nb, together with the corresponding elemental mapping images of Ni, Co, Mn, Al, and Nb for NCM-Al/Nb; TEM images and the corresponding FFT patterns of (c) NCM and (d) NCM-Al/Nb.

The surface morphologies and corresponding elemental distributions of NCM and NCM-Al/Nb are shown in Fig. 2a and b. Both samples consist of spherical secondary particles with sizes of approximately 10 μm, which are formed by the agglomeration of similar primary particles. Distinct surface deposits can be observed on the pristine NCM sample, whereas the NCM-Al/Nb sample exhibits a much smoother surface with fewer visible surface residues. This difference may be associated with the introduction of Al and Nb, which may reduce the amount of residual lithium-related species on the particle surface after calcination. This result is consistent with the surface composition analysis by XPS and suggests an improved surface state for the co-doped sample. In addition, elemental mapping of NCM-Al/Nb indicates that although the contents of Al and Nb are relatively low, both elements are uniformly distributed throughout the particles. To

further investigate the effect of Al/Nb co-modification on the local structure, TEM measurements were carried out for the NCM and NCM-Al/Nb samples, as shown in Fig. 2c and d. Clear lattice fringes can be observed in both samples, indicating good crystallinity. According to the lattice spacing measurements and fast Fourier transform (FFT) analysis, the observed lattice fringes can be assigned to the (003) planes. The interplanar spacing of the NCM sample is 0.468 nm, while that of the NCM-Al/Nb sample increases to 0.478 nm. This result is consistent with the trend obtained from the Rietveld refinement, confirming that Al/Nb co-modification can enlarge the interlayer spacing of the layered structure. The enlarged spacing is expected to facilitate Li^+ diffusion, in agreement with the subsequent GITT and EIS results.

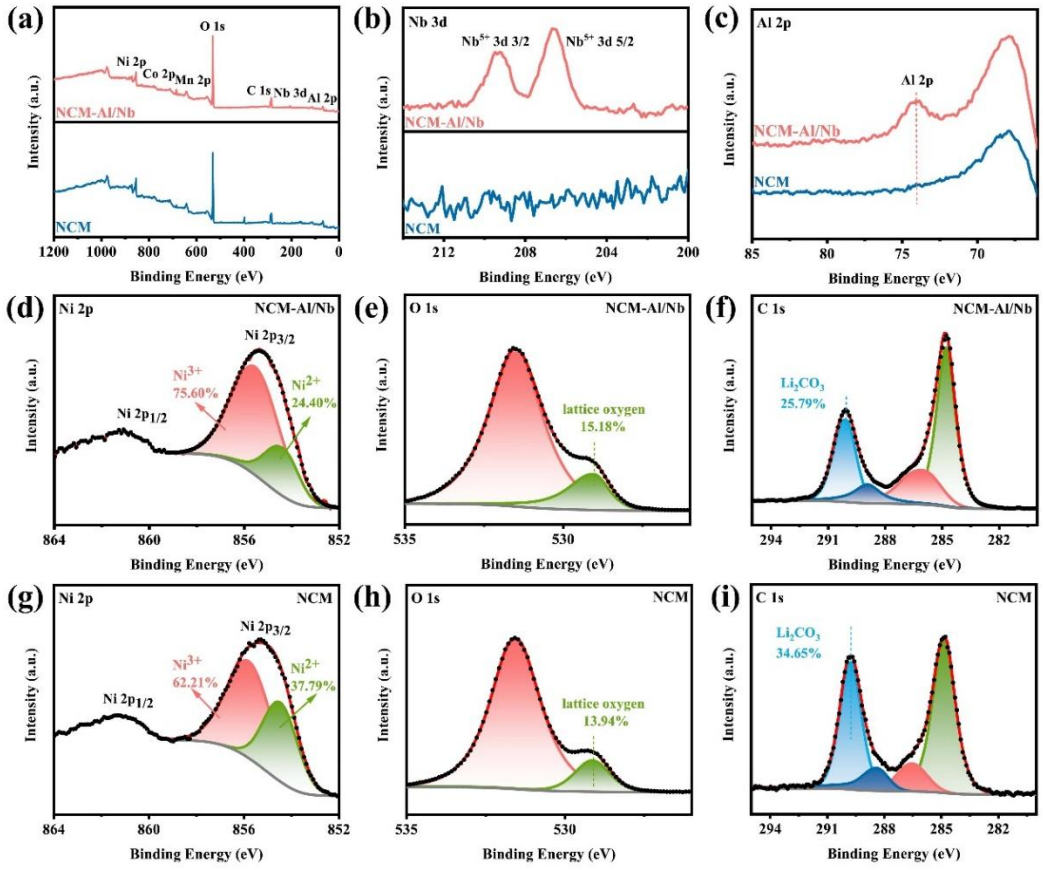


Fig. 3. XPS spectra of the samples: (a) survey spectrum; (b) Nb 3d and (c) Al 2p spectra of NCM-Al/Nb; (d–f) Ni 2p, O 1s, and C 1s spectra of NCM; and (g–i) Ni 2p, O 1s, and C 1s spectra of NCM-Al/Nb.

Fig. 3 presents the XPS results of NCM and NCM-Al/Nb, revealing the changes in surface chemical states after Al/Nb co-doping. For the NCM-Al/Nb sample, two

characteristic peaks located at 209.5 and 206.7 eV can be assigned to Nb 3d3/2 and Nb 3d5/2, respectively, indicating that Nb mainly exists in the Nb^{5+} state [41,42]. In addition, the peak detected at 74.5 eV corresponds to Al 2p, suggesting that Al is mainly present as Al^{3+} [43]. The Ni 2p spectrum consists of the Ni 2p1/2 and Ni 2p3/2 components. Deconvolution of the Ni 2p3/2 peak reveals the typical Ni^{2+} (854.3 eV) and Ni^{3+} (855.9 eV) species. The relative area of the Ni^{2+} component decreases from 37.79% for NCM to 24.40% for NCM-Al/Nb, indicating an increase in the average valence state of surface Ni after co-modification, which may be associated with a lower tendency for near-surface Li^{+}/Ni^{2+} disorder [44]. The C 1s spectra were further analyzed, and the fitted peak centered at around 289.7 eV is attributed to carbonate species. After Al/Nb incorporation, the relative area of this peak decreases from 34.65% to 25.79%, suggesting a reduced amount of residual lithium-related surface by-products [32]. The O 1s spectra can be deconvoluted into lattice oxygen-related and surface adsorbed oxygen-related components. The peak at approximately 529.1 eV is generally assigned to the lattice oxygen-related species. The relative area of this component increases from 13.94% to 15.18% after Al/Nb co-modification, implying a slightly more stable near-surface oxygen environment. This effect may be associated with the stronger Al-O and Nb-O bonding and may help alleviate interfacial side reactions and structural degradation during cycling [45,46].

3.2 Electrochemical performance

The initial charge/discharge curves of the four samples measured at 0.2 C within 2.7-4.3 V are shown in Fig. 4a. All samples display typical electrochemical characteristics of Ni-rich layered cathodes with relatively low polarization. The initial discharge specific capacities of NCM, NCM-Al, NCM-Nb, and NCM-Al/Nb are 203.61, 207.88, 210.11, and 208.59 mAh g^{-1}, respectively, with corresponding initial coulombic efficiencies of 84.08%, 84.66%, 85.42%, and 86.42%. The highest initial coulombic efficiency is obtained for NCM-Al/Nb, suggesting reduced irreversible capacity loss during the initial cycle. The cycling performances of the four samples at 1 C and 25 °C are shown in Fig. 4b. After 100 cycles, the pristine NCM retains a discharge capacity of 131.59 mAh g^{-1} with a capacity retention of 76.59%. In comparison, NCM-Al and

NCM-Nb deliver 146.79 and 143.99 mAh g^{-1}, corresponding to retentions of 82.66% and 80.29%, respectively. Among all samples, NCM-Al/Nb exhibits the best cycling stability, delivering 167.66 mAh g^{-1} after 100 cycles with a capacity retention of 89.21%. These results indicate that Al/Nb co-doping is more effective than single-element doping in improving cycling reversibility.

The discharge profiles of NCM and NCM-Al/Nb at different cycle numbers are presented in Fig. 4d and e. With prolonged cycling, both samples show a gradual shift of the discharge curves toward lower voltages, indicating increasing polarization. However, the pristine NCM exhibits a much faster decay of both discharge capacity and voltage plateau, whereas NCM-Al/Nb maintains a more stable discharge profile. A slight change in the discharge plateau of NCM-Al/Nb appears around the 75th cycle, and its origin requires further clarification. The long-term cycling performances of NCM and NCM-Al/Nb at 1 C are compared in Fig. 4f. After 160 cycles, NCM retains only 90.43 mAh g^{-1}, corresponding to 50.44% capacity retention. In contrast, NCM-Al/Nb still delivers 155.33 mAh g^{-1} with a capacity retention of 85.71%. Moreover, a rapid capacity decay is observed for NCM in the later stage of cycling, while no such abrupt fading is found for NCM-Al/Nb. This result suggests that Al/Nb co-doping effectively suppresses the structural and interfacial deterioration during prolonged cycling.

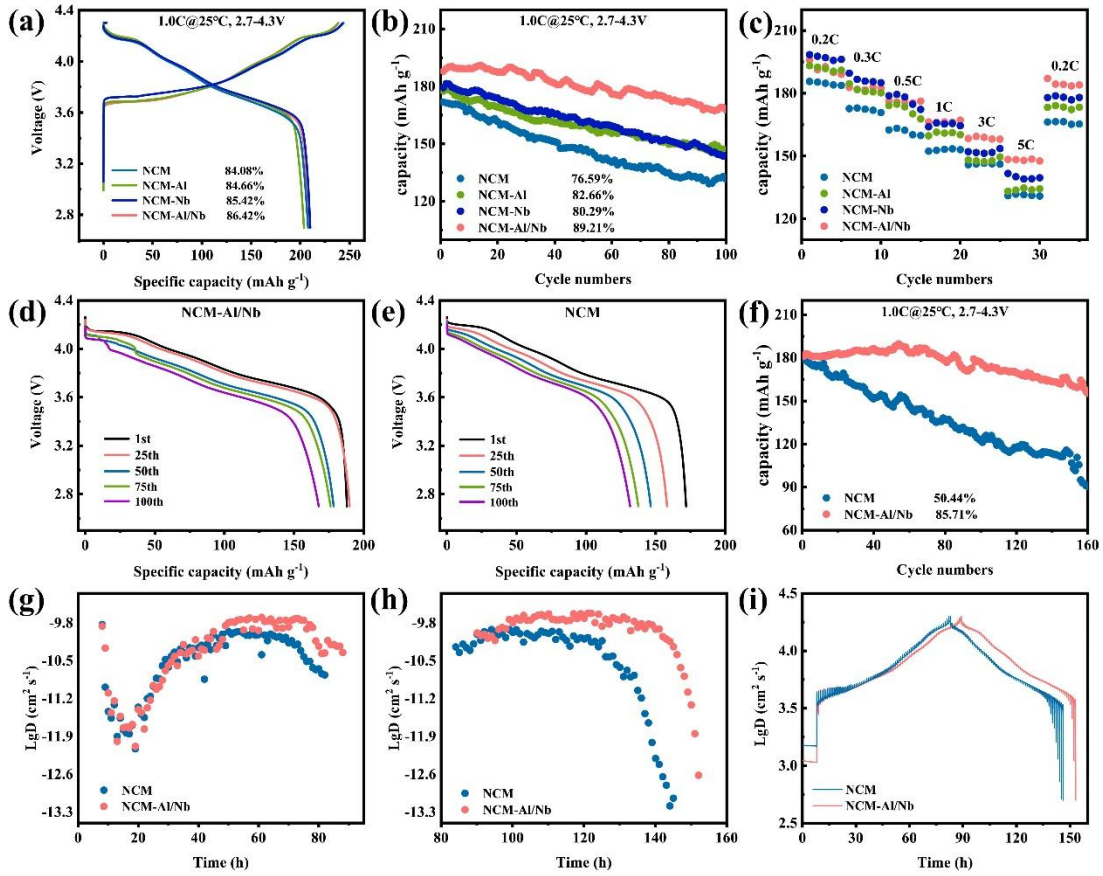


Fig. 4. (a) Initial charge–discharge curves of the four samples at 1 C; (b) cycling performance at 1 C for 100 cycles; (c) rate capability of the four samples; (d, e) discharge profiles of NCM and NCM-Al/Nb at different cycle numbers; (f) long-term cycling performance at 1 C for 160 cycles; and (g-i) GITT profiles and the corresponding Li^+ diffusion coefficients of NCM and NCM-Al/Nb.

The rate performances of the four samples are shown in Fig. 4c, and the detailed values are summarized in Table 1. As the current rate increases from 0.2 C to 5 C, the discharge capacities of all samples decrease gradually. Nevertheless, NCM-Al/Nb shows the best high-rate capability, especially at 1-5 C. At 5 C, NCM-Al/Nb still delivers 148.18 mAh g^{-1}, which is clearly higher than those of the other three samples. When the current rate returns to 0.2 C, NCM-Al/Nb shows the highest capacity recovery of 96.28%, compared with 89.83%, 90.33%, and 90.32% for NCM, NCM-Al, and NCM-Nb, respectively, indicating better structural reversibility and kinetic stability.

Table 1. Discharge capacities of the samples at different rates ($mAh \cdot g^{-1}$).

Sample	0.2C	0.3C	0.5C	1C	3C	5C	0.2C	Retention
NCM	184.72	172.15	161.62	152.96	146.21	131.28	165.94	89.83%
NCM-Al	191.84	181.63	172.08	160.70	148.09	133.99	173.28	90.33%
NCM-Nb	197.03	186.54	176.73	165.05	152.09	139.95	177.96	90.32%
NCM-Al/Nb	191.80	182.33	175.96	166.43	158.58	148.18	184.66	96.28%

The Li^+ diffusion kinetics of NCM and NCM-Al/Nb were further evaluated by GITT, as shown in Fig. 4g-i. The Li^+ diffusion coefficient (D_{Li^+}) was calculated according to the Weppner-Huggins equation [47]:

$$D_{Li+} = \frac{4L^2}{\pi\tau}\left[\frac{\Delta E_S}{\Delta E_\tau}\right]^2 \quad (1)$$

where L is the electrode thickness, τ is the pulse duration (600 s), ΔE_s is the steady state voltage change, and ΔE_τ is the voltage change during the current pulse. The average D_{Li^+} values of NCM during charge and discharge are 2.83×10^{-11} and 3.0×10^{-11} $cm^2\ s^{-1}$, respectively, while those of NCM-Al/Nb increase to 5.73×10^{-11} and 1.07×10^{-10} $cm^2\ s^{-1}$. Thus, the Li^+ diffusion coefficients of NCM-Al/Nb are enhanced by about 2 times during charge and 3.4 times during discharge. This improvement can be mainly ascribed to the enlarged interlayer spacing, reduced Li^+/Ni^{2+} cation-mixing tendency, and improved structural stability induced by Al/Nb co-doping [48].

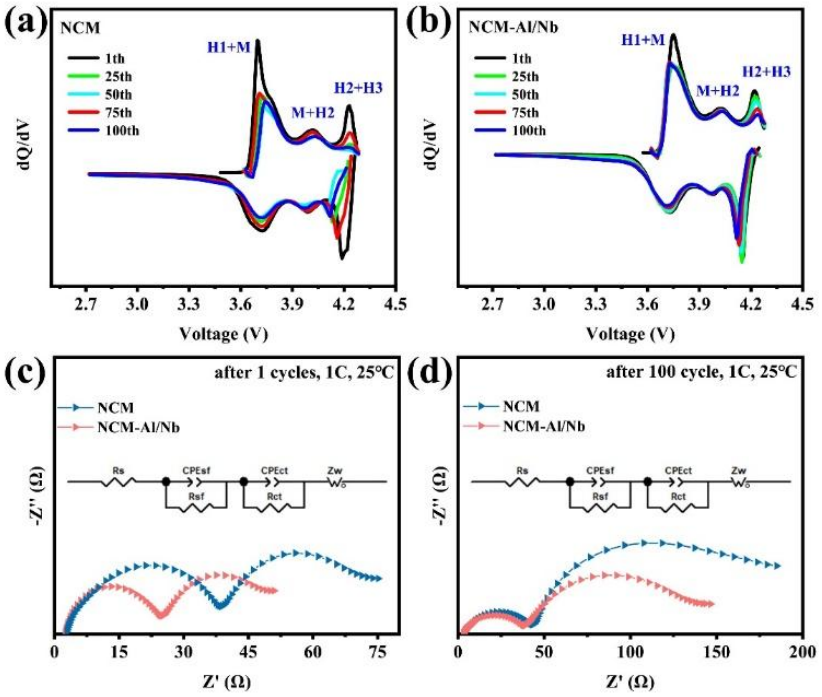


Fig. 5. (a, b) dQ/dV curves of NCM and NCM-Al/Nb at different cycle numbers; (c, d) EIS spectra of NCM and NCM-Al/Nb after the 1st and 100th cycles.

Ni-rich layered cathodes usually undergo multiple phase transitions during cycling, and differential capacity curves (dQ/dV) can effectively reflect the phase-transition behavior and polarization evolution of the electrode. Fig. 5a and b show the dQ/dV curves of NCM and NCM-Al/Nb collected after 1, 25, 50, 75, and 100 cycles at 1 C. Both samples exhibit the typical phase-transition sequence of H1→M→H2→H3. During cycling, the oxidation peak located at 4.1-4.3 V is generally associated with the H2–H3 phase transition. This transition is accompanied by pronounced lattice variation along the c-axis, which tends to induce internal stress accumulation and aggravate structural degradation and interfacial side reactions, thereby contributing to capacity fading in Ni-rich cathodes [36]. With increasing cycle number, the dQ/dV peaks of both samples gradually shift and weaken, indicating increased polarization and deteriorated electrochemical reversibility. In comparison, NCM-Al/Nb shows a higher degree of peak overlap and a smaller change in the H2–H3 peak intensity, suggesting better phase-transition reversibility and slower polarization growth during cycling. Combined with the above structural and surface analyses, this improvement can be mainly attributed to the reduced Li^{+}/Ni^{2+} cation-mixing tendency, enlarged interlayer spacing,

and more stable surface oxygen chemical environment induced by Al/Nb co-doping, which help alleviate stress accumulation during phase transition and enhance structural stability. EIS measurements were carried out on NCM and NCM-Al/Nb after the 1st and 100th cycles at 1 C, and the results are shown in Fig. 5c and d. The fitted impedance parameters are summarized in Table S2. With prolonged cycling, the R_s values of both samples increase, which may be related to electrolyte decomposition and interfacial evolution. In comparison, NCM-Al/Nb exhibits lower R_{sf} values before and after cycling, indicating that the growth of interphase-related resistance is effectively suppressed. Moreover, after 100 cycles, the R_{ct} value of NCM-Al/Nb remains significantly lower than that of NCM, confirming improved charge-transfer kinetics after Al/Nb co-modification.

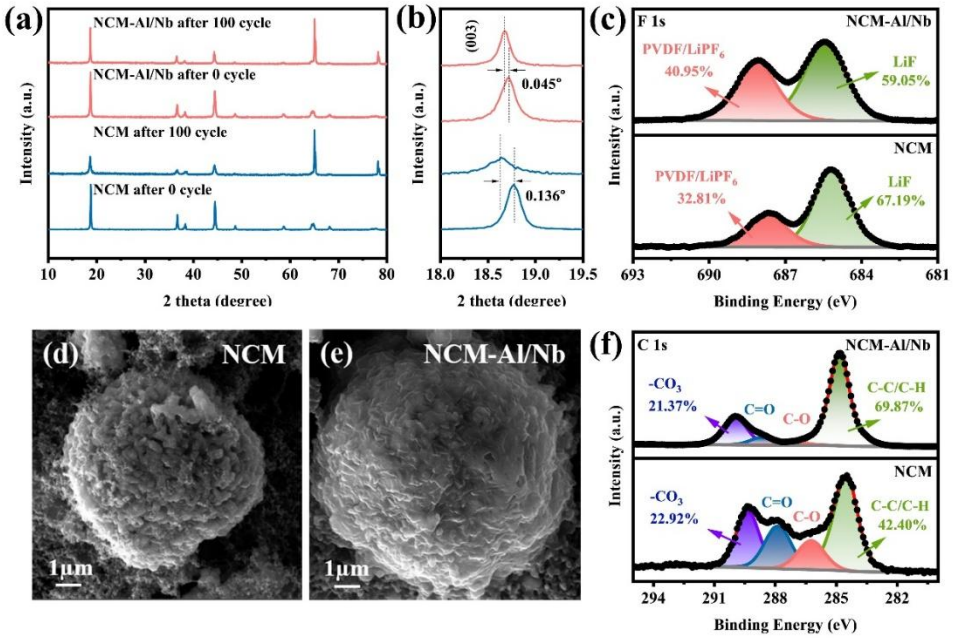


Fig. 6. Post-cycling characterization of NCM and NCM-Al/Nb after 100 cycles: (a, b) XRD patterns, (c, f) XPS spectra, and (d, e) SEM images.

To further clarify the effect of Al/Nb co-doping on the post-cycling structural and interfacial stability, XRD, SEM, and XPS analyses were performed on NCM and NCM-Al/Nb after 100 cycles at 1 C and 25 °C. The XRD patterns before and after cycling, together with the enlarged view of the (003) peak, are shown in Fig. 6a and b. After 100 cycles, the (003) peaks of both samples shift toward lower angles, indicating irreversible structural changes during cycling. The peak shift of the pristine NCM

reaches 0.136°, whereas that of NCM-Al/Nb is only 0.045º, suggesting that Al/Nb co-doping is effective in maintaining the layered structure and suppressing abnormal lattice variation upon cycling. Compared with NCM, the smaller shift of the (003) peak in NCM-Al/Nb indicates less structural deterioration during repeated charge/discharge processes. The SEM images in Fig. 6d and e further support the above XRD results. After 100 cycles, the NCM sample exhibits a much rougher surface, accompanied by fine particle detachment and loose secondary-particle aggregation, indicating obvious structural damage during cycling. In contrast, NCM-Al/Nb largely retains an intact spherical morphology without severe cracking or pulverization, suggesting that Al/Nb co-doping helps alleviate cycling-induced structural degradation. Combined with the dQ/dV analysis, this improvement may be related to the mitigation of stress accumulation associated with the H2–H3 phase transition. The XPS results of the cycled samples are shown in Fig. 6c and f. Compared with NCM, NCM-Al/Nb exhibits lower relative contents of the C=O and C−O species associated with the cathode electrolyte interphase (CEI), and the LiF-related component decreases from 67.19% to 59.05%. These results suggest less accumulation of interfacial by-products and suppressed interphase growth on the co-doped sample after cycling. This observation is consistent with its lower interfacial resistance and improved Li^+ transport kinetics [49,50]. To further highlight the competitiveness of the present work, the electrochemical performance of NCM-Al/Nb is compared with several representative reported Ni-rich cathode materials in Table S3. Although the testing conditions are not completely identical among different studies, the NCM-Al/Nb sample in this work still delivers a relatively high capacity retention of 85.71% after 160 cycles at 1 C within the 2.7-4.3 V window, demonstrating the effectiveness of the Al/Nb co-modification strategy for improving the cycling stability of Ni-rich layered cathodes.

4 Conclusion

An Al/Nb co-modified Ni-rich layered cathode, $LiM_{0.98}Al_{0.01}Nb_{0.01}O_2$, was synthesized and systematically investigated in this work. The results show that Al/Nb co-doping preserves the layered structure, improves structural ordering, enlarges the interlayer spacing, and reduces the Li^+/Ni^{2+} cation-mixing tendency, thereby promoting

Li^+ diffusion kinetics. As a result, NCM-Al/Nb exhibits excellent cycling stability and rate capability, delivering a capacity retention of 85.71% after 160 cycles at 1 C and a discharge specific capacity of 148.18 mAh g^{-1} at 5 C. Post-cycling analyses further indicate that Al/Nb co-doping helps suppress structural degradation and interfacial side reactions. This work demonstrates that synergistic Al/Nb co-modification is an effective strategy for improving the overall performance of low-Co/high-Ni layered cathodes.

CRediT authorship contribution statement

Chengzhou Li: Data processing and analysis, Results discussion, Original draft preparation. **Xingrong Hu**: Data processing and analysis, Original draft preparation. **Chunxiang Wang**: Results discussion, Paper revision and polishing. **Hao Zheng:** Data analysis, Data analysis, Results discussion. **Yichen Song:** Data processing and analysis, Original draft preparation. **Zhifeng Li**: Results discussion, Paper revision and polishing, Equipment supply.

Declaration of competing interest

The authors declare that they have no known competing financial interests or personal relationships that could have appeared to influence the work reported in this paper.

Data availability

Data will be made available on request.

Acknowledgements

This work was supported by Jiangxi Natural Science Foundation (no. 20232BAB204027), and Open Project of the Jiangxi Provincial Key Laboratory of Power Batteries & Energy Storage Materials (2024SSY1001102).

References

1 S. W. Woo, S. T. Myung, H. Bang, D. W. Kim and Y. K. Sun, Improvement of electrochemical and thermal properties of $Li[N_{i0.8}Co_{0.1}Mn_{0.1}]O_2$ positive electrode materials by multiple metal (Al, Mg) substitution, Electrochim. Acta, 2009, 54(15), 3851–3856, DOI: 10.1016/j.electacta.2009.01.048.

2 H. Z. Zhang, C. Liu, D. W. Song, L. Q. Zhang and L. J. Bie, A new synthesis strategy towards enhancing the structure and cycle stabilities of the $LiNi_{0.80}Co_{0.15}Al_{0.05}O_2$ cathode material, J. Mater. Chem. A, 2017, 5(2), 835–841, DOI: 10.1039/C6TA08084G.

3 Y. Shen, L. Wang, J. Jiang, D. Wang, D. Zhang, D. Yin, L. Wang, X. Zhang, G. Huang and Y. Cheng, Stabilization of high-voltage layered oxide cathode by multi-electron rare earth oxide, Chem. Eng. J., 2023, 454, 140249, DOI: 10.1016/j.cej.2022.140249.

4 K. Du, J. L. Huang, Y. B. Cao, Z. D. Peng and G. R. Hu, Study of effects on $LiNi_{0.8}Co_{0.15}Al_{0.05}O_2$ cathode by $LiNi_{1/3}Co_{1/3}Mn_{1/3}O_2$ coating for lithium ion batteries, J. Alloys Compd., 2013, 574, 377–382, DOI: 10.1016/j.jallcom.2013.05.134.

5 W. Xiao, J. Y. Wang, L. L. Fan, J. J. Zhang and X. F. Li, Recent advances in $Li_{1+x}Al_xTi_{2-x}(PO_4)_3$ solid-state electrolyte for safe lithium batteries, Energy Storage Mater., 2019, 19, 379–400, DOI: 10.1016/j.ensm.2018.10.012.

6 G. Harper, R. Sommerville, E. Kendrick, L. Driscoll, P. Slater, R. Stolkin, A. Walton, P. Christensen, O. Heidrich, S. Lambert, A. Abbott, K. Ryder, L. Gaines and P. Anderson, Recycling lithium-ion batteries from electric vehicles, Nature, 2019, 575(7781), 75–86, DOI: 10.1038/s41586-019-1682-5.

7 F. Duffner, N. Kronemeyer, J. Tübke, J. Leker, M. Winter and R. Schmuch, Post-lithium-ion battery cell production and its compatibility with lithium-ion cell production infrastructure, Nat. Energy, 2021, 6(2), 123–134, DOI: 10.1038/s41560-020-00748-8.

8 T. F. Yi, T. T. Wei, Y. Li, Y. B. He and Z. B. Wang, Efforts on enhancing the Li-ion diffusion coefficient and electronic conductivity of titanate-based anode materials for advanced Li-ion batteries, Energy Storage Mater., 2020, 26, 165–197, DOI: 10.1016/j.ensm.2019.12.042.

9 D. D. Liu, C. Chen and X. H. Xiong, Research progress on artificial protective films for lithium metal anodes, Chin. J. Inorg. Chem., 2021, 37(2), 1–15, DOI: 10.3866/PKU.WHXB202008078.

10 C. L. Xu, W. Xiang, Z. G. Wu, L. Qiu, Y. Ming, W. Yang, L. C. Yue, J. Zhang, B. H. Zhong, X. D. Guo, G. K. Wang and Y. X. Liu, Dual-site lattice modification regulated cationic ordering for Ni-rich cathode towards boosted structural integrity and cycle stability, Chem. Eng. J., 2021, 403, 126314, DOI: 10.1016/j.cej.2020.126314.

11 Y. L. Wang, X. Huang, F. Li, J. S. Cao and S. H. Ye, Enhanced high rate performance of $Li[Li_{0.17}Ni_{0.2}Co_{0.05}Mn_{0.58-x}Al_x]O_{2-0.5x}$ cathode material for lithium-ion batteries, RSC Adv., 2015, 5(61), 49651–49656, DOI: 10.1039/C5RA03971A.

12 W. R. Li, H. Zhuang, L. J. Guo, Y. Chen, X. Y. Liu, B. B. Li, B. Zhao, Y. Jiang and J. J. Zhang, Improvement of cycling stability and high-temperature performance of $Li[Ni_{0.80}Co_{0.15}Al_{0.05}]O_2$ cathode by thin-layer AlF_3 coating, J. Mater. Sci.: Mater. Electron., 2020, 31(14), 11141–11149, DOI: 10.1007/s10854-020-03663-6.

13 F. Lin, I. M. Markus, D. Nordlund, T. C. Weng, M. D. Asta, H. L. Xin and M. M. Doeff, Surface reconstruction and chemical evolution of stoichiometric layered cathode materials

for lithium-ion batteries, Nat. Commun., 2014, 5, 4529, DOI: 10.1038/ncomms4529.
14 M. D. Radin, S. Hy, M. Sina, C. Fang, H. Liu, J. Vinckeviciute, M. Zhang, M. S. Whittingham, Y. S. Meng and A. Van der Ven, Narrowing the gap between theoretical and practical capacities in Li-ion layered oxide cathode materials, Adv. Energy Mater., 2017, 7, 1602888, DOI: 10.1002/aenm.201602888.
15 H. Li, P. F. Zhou, F. M. Liu, H. X. Li, F. Y. Cheng and J. Chen, Stabilizing nickel-rich layered oxide cathodes by magnesium doping for rechargeable lithium-ion batteries, Chem. Sci., 2019, 10(5), 1374–1379, DOI: 10.1039/C8SC03385D.
16 S. Xu, C. Y. Du, X. Xu, G. K. Han, P. J. Zuo, X. Q. Cheng, Y. L. Ma and G. P. Yin, A mild surface washing method using protonated polyaniline for Ni-rich $LiNi_{0.8}Co_{0.1}Mn_{0.1}O_2$ material of lithium-ion batteries, Electrochim. Acta, 2017, 248, 534–540, DOI: 10.1016/j.electacta.2017.07.169.
17 W. M. Seong and A. Manthiram, Complementary effects of Mg and Cu incorporation in stabilizing the cobalt-free $LiNiO_2$ cathode for lithium-ion batteries, ACS Appl. Mater. Interfaces, 2020, 12(39), 43653–43664, DOI: 10.1021/acsami.0c11413.
18 P. F. Yan, J. M. Zheng, M. Gu, J. Xiao, J. G. Zhang and C. M. Wang, Intragranular cracking as a critical barrier for high-voltage usage of layer-structured cathode for lithium-ion batteries, Nat. Commun., 2017, 8, 14101, DOI: 10.1038/ncomms14101.
19 H. Liu, M. Wolfman, K. Karki, Y. S. Yu, E. A. Stach, J. Cabana, K. W. Chapman and P. J. Chupas, Intergranular cracking as a major cause of long-term capacity fading of layered cathodes, Nano Lett., 2017, 17(6), 3452–3457, DOI: 10.1021/acs.nanolett.7b00379.
20 H. H. Zheng, X. X. Li, Z. Huang, X. Q. Yang, J. H. Deng, G. Q. Zhang and X. W. Tang, Investigation of the performance and recession mechanisms of high-nickel ternary lithium-ion batteries under artificial aging discharge rates, Energy Technol., 2022, 10(11), 2200600, DOI: 10.1002/ente.202200600.
21 Y. Tang, J. P. Zhao, L. J. Xie, Q. T. Ke, C. Liang, J. C. Jiang and A. C. Huang, Electrochemical performance and thermal stability of Co_3O_4 modified high nickel ternary cathode materials, J. Loss Prev. Process Ind., 2026, 100, 105901, DOI: 10.1016/j.jlp.2025.105901.
22 Z. C. Yi, C. J. Liu, C. Miao, Z. Y. Wang, J. L. Wang, Y. Xin and W. Xiao, In-situ Ti^{4+}-doped modification of layer-structured Ni-rich $LiNi_{0.83}Co_{0.11}Mn_{0.06}O_2$ cathode materials for high-energy lithium-ion batteries, J. Colloid Interface Sci., 2025, 677, 91–100, DOI: 10.1016/j.jcis.2024.08.064.
23 A. Saleem, A. Hussain, M. Z. Ashfaq, M. S. Javed, S. Rauf, M. M. Hussain, A. Saad, J. Shen, M. K. Majeed and R. Iqbal, A well-controlled cracks and gliding-free single-crystal Ni-rich cathode for long-cycle-life lithium-ion batteries, J. Alloys Compd., 2022, 924, 166375, DOI: 10.1016/j.jallcom.2022.166375.
24 T. C. Liu, L. Yu, J. Lu, T. Zhou, X. J. Huang, Z. H. Cai, A. Dai, J. Gim, Y. Ren, X. H. Xiao, M. V. Holt, Y. S. Chu, I. Arslan, J. G. Wen and K. Amine, Rational design of mechanically robust Ni-rich cathode materials via concentration gradient strategy, Nat. Commun., 2021, 12(1), 6024, DOI: 10.1038/s41467-021-26290-z.
25 Y. K. Lei, J. J. Ai, S. Yang, C. Y. Lai and Q. J. Xu, Nb-doping in $LiNi_{0.8}Co_{0.1}Mn_{0.1}O_2$ cathode material: effect on the cycling stability and voltage decay at high rates, J. Taiwan Inst. Chem. Eng., 2019, 97, 255–263, DOI: 10.1016/j.jtice.2019.02.006.

26 Y. Li, Y. Huang, J. Li, C. Lei, Z. He, Y. Cheng, F. Wu and Y. Li, B-doped nickel-rich ternary cathode material for lithium-ion batteries with excellent rate performance, Ionics, 2023, 29(11), 4559–4567, DOI: 10.1007/s11581-023-05191-9.

27 Y. Lv, X. Cheng, W. Qiang and B. Huang, Improved electrochemical performances of Ni-rich $LiNi_{0.83}Co_{0.12}Mn_{0.05}O_2$ by Mg-doping, J. Power Sources, 2020, 450, 227718, DOI: 10.1016/j.jpowsour.2020.227718.

28 Z. Ren, C. Shen, M. Liu, J. Liu, S. Zhang, G. Yang, L. Huai, X. Liu, D. Wang and H. Li, Improving $LiNi_{0.9}Co_{0.08}Mn_{0.02}O_2$'s cyclic stability via abating mechanical damages, Energy Storage Mater., 2020, 28, 1–9, DOI: 10.1016/j.ensm.2020.02.028.

29 M. Jeong, H. Kim, W. Lee, S. J. Ahn, E. Lee and W. S. Yoon, Stabilizing effects of Al-doping on Ni-rich $LiNi_{0.8}Co_{0.15}Mn_{0.05}O_2$ cathode for Li rechargeable batteries, J. Power Sources, 2020, 474, 228592, DOI: 10.1016/j.jpowsour.2020.228592.

30 K. Zhou, Q. Xie, B. H. Li and A. Manthiram, An in-depth understanding of the effect of aluminum doping in high-nickel cathodes for lithium-ion batteries, Energy Storage Mater., 2021, 34, 229–240, DOI: 10.1016/j.ensm.2020.09.015.

31 K. K. Lee, W. S. Yoon, K. B. Kim, K. Y. Lee and S. T. Hong, Characterization of $LiNi_{0.85}Co_{0.10}M_{0.05}O_2$ (M = Al, Fe) as a cathode material for lithium secondary batteries, J. Power Sources, 2001, 97–98, 308–312, DOI: 10.1016/S0378-7753(01)00516-X.

32 Y. C. Li, W. Xiang, Z. G. Wu, C. L. Xu, Y. D. Xu, Y. Xiao, Z. G. Yang, C. J. Wu, G. P. Lv and X. D. Guo, Construction of homogeneously Al^{3+} doped Ni-rich Ni-Co-Mn cathode with high stable cycling performance and storage stability via scalable continuous precipitation, Electrochim. Acta, 2018, 291, 84–94, DOI: 10.1016/j.electacta.2018.08.124.

33 C. C. Sun, W. X. Chen, P. Gao, H. L. Hu, J. G. Zheng and Y. M. Zhu, Investigation of structure and cycling performance of Nb-doped nickel-rich single-crystal ternary cathode materials, Ionics, 2022, 28(2), 747–757, DOI: 10.1007/s11581-021-04293-6.

34 J. Wang, Z. Yi, C. Liu et al., Revealing the effect of Nb^{5+} on the electrochemical performance of nickel-rich layered $LiNi_{0.83}Co_{0.11}Mn_{0.06}O_2$ oxide cathode for lithium-ion batteries, J. Colloid Interface Sci., 2023, 635, 295–304, DOI: 10.1016/j.jcis.2022.12.142.

35 T. T. Zhao, P. Liu, F. L. Tang, M. Z. Xiao, L. B. Song, Y. J. Kuang, T. Y. Long and Z. L. Xiao, Design of Nb^{5+}-doped high-nickel layered ternary cathode material and its structure stability, Nanotechnology, 2023, 34(49), 495401, DOI: 10.1088/1361-6528/acf670.

36 X. R. Zhang, L. Cao, H. Q. Sun, C. C. Zhao, S. Tian, J. Song, L. M. Luo and Y. C. Wu, Research on the bifunctional mechanism of Cr_8O_{21} active coating in synergistically regulating structural stability and interface kinetics of high-nickel NCM811, J. Alloys Compd., 2025, 1039, 182817, DOI: 10.1016/j.jallcom.2025.182817.

37 Z. L. Gong, H. S. Liu, X. J. Guo, Z. R. Zhang and Y. Yang, Effects of preparation methods of $LiNi_{0.8}Co_{0.2}O_2$ cathode materials on their morphology and electrochemical performance, J. Power Sources, 2004, 136(1), 139–144, DOI: 10.1016/j.jpowsour.2004.05.022.

38 Y. X. Sun, C. X. Hai, Y. Shen, J. B. Zeng, L. J. Zhang, X. Li, X. F. Ren, S. D. Dong, G. T. Zhang, C. Sun and Y. Zhou, Improved lithium-ion diffusion and stability of a $LiNi_{0.8}Co_{0.1}Mn_{0.1}O_2$ cathode via the synergistic effect of Na and Mg dual-metal cations for lithium ion battery, J. Electrochem. Soc., 2020, 167(2), 020522, DOI: 10.1149/1945-7111/ab6977.

39 Y. J. Guo, C. H. Zhang, S. Xin, J. L. Shi, W. P. Wang, M. Fan, Y. X. Chang, W. H. He, E.

Wang, Y. G. Zou, X. Yang, F. Meng, Y. Y. Zhang, Z. Q. Lei, Y. X. Yin and Y. G. Guo, Competitive doping chemistry for nickel-rich layered oxide cathode materials, Angew. Chem., Int. Ed., 2022, 61(21), e202116865, DOI: 10.1002/anie.202116865.

40 Z. H. Wang, S. X. Zhuang, G. X. Sun, X. X. Pan, J. Y. He, Y. Q. Sun, S. Y. Jiang and Y. Ren, Stabilization of NCM811 cathode for Li-ion batteries by N-doped carbon coating, Diamond Relat. Mater., 2023, 138, 110233, DOI: 10.1016/j.diamond.2023.110233.

41 M. Jiang, C. X. Tian, D. H. Wang, X. C. Wu, W. S. Yan and C. G. Chen, Mechanically stabilized Ni-rich cathode via niobium-integrated architecture engineering for high-voltage fast-charging lithium-ion batteries, Energy Storage Mater., 2026, 84, 104829, DOI: 10.1016/j.ensm.2025.104829.

42 Y. J. Kim, R. Rajagopal, S. Kang and K. S. Ryu, Novel dry deposition of $LiNbO_3$ or Li_2ZrO_3 on $LiNi_{0.6}Co_{0.2}Mn_{0.2}O_2$ for high-performance all-solid-state lithium batteries, Chem. Eng. J., 2020, 386, 123975, DOI: 10.1016/j.cej.2019.123975.

43 Y. Tao, Y. Lu, Y. J. Guo, J. M. Guo, M. W. Xiang, W. Bai, X. F. Liu and H. L. Bai, Facile synthesis and electrochemical properties of truncated octahedral Al, Ni dual doped $LiMn_2O_4$ cathode materials, J. Alloys Compd., 2022, 904, 164027, DOI: 10.1016/j.jallcom.2022.164027.

44 Z. H. Yu and B. X. Huang, Synergistic enhancement of high-nickel $LiNi_{0.83}Co_{0.11}Mn_{0.06}O_2$ cathode performance via Ti doping and $Li_{7.3}La_3Zr_{1.7}Co_{0.3}O_{12}$ mixed ionic-electronic conductor coating, J. Alloys Compd., 2025, 1037, 182263, DOI: 10.1016/j.jallcom.2025.182263.

45 Y. Wang, C. X. Xu, X. T. Tian, S. Y. Wang and Y. Zhao, Challenges and modification strategies of high-voltage cathode materials for Li-ion batteries, CJSC, 2023, 42(10), 100167, DOI: 10.1016/j.cjsc.2023.100167.

46 Y. Levartovsky, A. Chakraborty, S. Kunnikuruvan, S. Maiti, J. Grinblat, M. Talianker, D. Aurbach and D. Thomas, High-energy Ni-rich $LiNi_{0.85}Co_{0.1}Mn_{0.05}O_2$ cathode material for Li-ion batteries enhanced by Nd- and Y-doping: a structural, electrochemical, and thermal investigation, ACS Appl. Energy Mater., 2022, 5(9), 11142–11151, DOI: 10.1021/acsaem.2c01731.

47 W. J. Ge, L. Bai and X. Li, Effects of reheating temperature on the structure, morphology and electrochemical performance of Ni-rich cathode materials, J. Alloys Compd., 2021, 876, 160098, DOI: 10.1016/j.jallcom.2021.160098.

48 L. Y. Lin, W. Guo, Y. X. Pan, Y. H. Tian, N. Tan, H. Liu, C. H. An, Q. B. Deng and N. Hu, Boosting high-voltage performance of single-crystal NCM811 cathode by the synergistic effect of Nb doping and Al_2O_3 coating, J. Alloys Compd., 2025, 1036, 181725, DOI: 10.1016/j.jallcom.2025.181725.

49 L. C. Li, M. L. Liu, P. Yang, W. F. Yuan and J. Chen, Tris(pentafluoro)phenylborane electrolyte additive regulates highly stable and uniform CEI membrane components to improve the high-voltage behaviors of NCM811 lithium-ion batteries, J. Colloid Interface Sci., 2024, 676, 613–625, DOI: 10.1016/j.jcis.2024.07.155.

50 P. He, M. L. Zhang, J. Wu, Y. J. Li, Y. Wang, Y. X. Yan, D. Y. Zhang and X. F. Sun, Enhanced cyclic stability and discharge capacity of NCM811 cathode by coating ferroelectric-type $LiNbO_3$ ionically conductive layer, J. Alloys Compd., 2023, 967, 171822, DOI: 10.1016/j.jallcom.2023.171822.

Supplementary Files

This is a list of supplementary files associated with this preprint. Click to download.

- SupportingInformationionics.docx